PHYSICAL REVIEW MATERIALS **9**, 054607 (2025)

Effects of strain compensation on electron mobilities in InAs quantum wells grown on InP(001)

C. P. Dempsey,[1,*] J. T. Dong,[2] I. Villar Rodriguez,[3] Y. Gul,[3] S. Chatterjee,[1] M. Pendharkar,[1,†] S. N. Holmes,[4]
M. Pepper,[3,4] and C. J. Palmstrøm[1,2,‡]
[1]*Department of Electrical and Computer Engineering, University of California, Santa Barbara, California 93106, USA*
[2]*Materials Department, University of California Santa Barbara, Santa Barbara, California 93106, USA*
[3]*London Centre for Nanotechnology, University College London, 17-19 Gordon Street, London WC1H 0AH, United Kingdom*
[4]*Department of Electronic and Electrical Engineering, University College London, Torrington Place, London WC1E 7JE, United Kingdom*

(Received 27 June 2024; revised 6 March 2025; accepted 23 April 2025; published 27 May 2025)

InAs quantum wells (QWs) grown on InP substrates are interesting for their applications in devices with high spin-orbit coupling and their potential role in creating topologically nontrivial hybrid heterostructures. These QWs rely on InGaAs cladding layers and InAlAs barrier layers to confine electrons within a thin InAs well. The highest mobility QWs are limited by interfacial roughness scattering and alloy disorder scattering in the cladding and barrier layers. Increasing QW thickness has been shown to reduce the effect of both of these scattering mechanisms. However, for current state-of-the-art devices with As-based cladding and barrier layers, the critical thickness is limited to $\leqslant 7$ nm. In this paper, we demonstrate the use of strain compensation techniques in the $In_xGa_{1-x}As$ cladding layers, grown on $In_{0.81}Al_{0.19}As$ barrier layers, to extend the critical thickness well beyond this limit. We induce tensile strain in the InGaAs cladding layers by reducing the In concentration from $In_{0.81}Ga_{0.19}As$ to $In_{0.70}Ga_{0.30}As$ and we observe changes in both the critical thickness of the well and the maximum achievable mobility. The peak electron mobility at 2 K is 1.16×10^6 cm^2/V s, with a carrier density of 4.2×10^{11} cm^{-2}. Additionally, we study the quantum lifetime and Rashba spin splitting in the highest mobility device as these parameters are critical to determine if these structures can be used in topologically nontrivial devices.

DOI: 10.1103/PhysRevMaterials.9.054607

I. INTRODUCTION

Bulk InAs has a Landé g factor of 15 [1], making it a useful material for studying large spin-orbit coupling in devices. Additionally, quantum wells (QWs) of InAs have high mobilities ($>1 \times 10^6$ cm^2/V s) [2–4] and near surface QWs have demonstrated gateable induced superconductivity [5], making them an ideal platform for the study of topologically nontrivial hybrid heterostructures. InAs quantum wells have been grown on GaAs, InP, and nearly lattice-matched GaSb substrates. A record mobility of 2.4×10^6 cm^2/V s was achieved in a 21-nm-thick InAs QW utilizing Sb-based barriers ($Al_xGa_{1-x}Sb$ and/or AlSb barrier layers [3,4]), a GaSb substrate, and by tuning the carrier density to $n_s \sim 1 \times 10^{12}$ [4]. Shojaei *et al.* [6] demonstrated that interface roughness was one of the dominant scattering mechanisms at high carrier densities and that these effects could be mitigated by increasing the QW width, leading to an increase in the maximum mobility. Sb-based InAs QW structures are utilized because the cladding layers, barrier layers, and substrate are all nearly lattice matched with the InAs layer, increasing the critical thickness of the QW. However, when Hall bar devices are fabricated, InAs QWs with Sb-based cladding and barrier layers typically suffer from side-wall conduction [7]. Different methods of passivation have been experimented with, but the trivial edge conductance could not be completely removed from the transport spectra [8].

Trivial edge conductance is not observed for Hall bars of InAs QWs with As-based cladding and barrier layers. However, these structures are typically grown on an InP substrate. InAs grown pseudomorphically on InP is under a compressive strain of −3.1%. This large lattice mismatch requires the use of metamorphic buffer layers to increase the in-plane lattice constant of the film surface while minimizing the nucleation of threading dislocations. Buffer layer engineering has enabled these QWs to reach a record mobility of $\mu = 1.1 \times 10^6$ cm^2/V s at a carrier density of $n_s = 6.2 \times 10^{11}$ cm^{-2} [2], minimizing the difference between InAs QWs grown on InP substrates and InAs QWs grown on GaSb substrates. However, these current state-of-the-art InAs QWs grown on InP are limited to thicknesses of 4 nm due to the in-plane lattice constant difference between the InAs layer and the surrounding $In_xGa_{1-x}As$ cladding and $In_xAl_{1-x}As$ barrier layers. When more than 4 nm of InAs is grown on an $x = 0.75$ In-containing active region, the QW begins to relax, lowering the sample mobility [2]. Previous work [5,9] has demonstrated that by increasing the In concentration of the $In_xGa_{1-x}As$ cladding/$In_xAl_{1-x}As$ barrier layers from $x = 0.75$ to $x = 0.81$, the critical thickness of the InAs layer can be increased up to 7 nm. Additionally, Benali *et al.* [9]

---

[*] Contact author: c_dempsey@ucsb.edu

[†] Present address: Department of Materials Science and Engineering, Stanford University, Stanford, CA 94305.

[‡] Contact author: cjpalm@ucsb.edu

demonstrated this increase leads to a higher fraction of the two-dimensional (2D) electron gas (2DEG) being confined within the InAs layer, lowering its penetration into the cladding and barrier layers and reducing the effects of alloy disorder and interfacial roughness scattering. In doing so, they proceeded to break the record for the highest mobility of InAs QWs grown on a GaAs substrate [9]. While further increases in the In content of the barrier and cladding layers would enable thicker InAs QWs, it would also decrease QW confinement, potentially leading to an increase in scattering and minimizing any potential benefits.

Strain compensation provides another pathway to increase QW critical thickness beyond the current technical limits of 7 nm without sacrificing 2DEG confinement. Early uses of strain compensation include increasing the maximum number of QWs in multi-quantum-well structures [10–12] by growing InGaAsP layers under tensile strain to counteract the compressive strain of the $In_{0.67}Ga_{0.33}As$ QW layers. This produced a zero net strain structure and demonstrated the promise of strain compensation in increasing critical thickness. In this paper we discuss the effects of implementing strain compensation by tuning the In concentration of the cladding layers ($In_xGa_{1-x}As$ layers) and the impact that strain compensation has on both the maximum thickness of the QW and the maximum mobility of the heterostructure.

II. METHODS

The QW samples studied in this paper were grown by molecular beam epitaxy (MBE) in a VG V80H growth chamber. Fe-doped InP (001) semi-insulating epiready substrates were purchased from AXT Inc. The native oxide on the InP substrate was thermally desorbed by heating the substrate under an As_2 flux; a valved cracker source was used to generate the As_2 flux for the entire duration of the growth. The surface reconstruction was monitored during this process using reflection high energy electron diffraction (RHEED). The transition to the metal rich (4×2) reconstruction was used to calibrate the pyrometer temperature to 515 °C and, upon observing the transition, the sample temperature was immediately reduced to 480 °C for the nucleation of a lattice-matched $In_{0.52}Al_{0.48}As/In_{0.53}Ga_{0.47}As$ superlattice. After growth of the superlattice, the sample temperature was further reduced to 340 °C to grow the step graded buffer layers (SGBL). Each layer of the SGBL is 50 nm thick and the In concentration is increased by 2.5% for each step, up to $In_{0.80}Al_{0.20}As$. Next, a 400 nm overstep layer of $In_{0.83}Al_{0.17}As$ was grown to fully relieve residual strain in the SGBL. Finally, a 100 nm layer of $In_{0.81}Al_{0.19}As$ was grown, utilizing the same composition as Benali *et al.* [9] for the active region. At this point, growth of the active region of the QW commenced and the substrate was heated to 450 °C.

A 60-nm-thick $In_{0.81}Al_{0.19}As$ bottom barrier layer was grown with a 10-nm-thick $In_xGa_{1-x}As$ bottom cladding layer grown subsequently. The strain in the cladding layers was modified by changing x from $x = 0.81$ to 0.74, 0.72, or 0.70. By reducing x, the lattice constant of the $In_xGa_{1-x}As$ decreases relative to the $In_{0.81}Al_{0.19}As$ bottom barrier, leading to an accumulation of tensile strain energy within the cladding layer. Next, the InAs QW, which will always be under compressive strain in these structures, was grown with thickness, t_{QW}. By varying the lattice constant of the cladding layers, t_{QW} was increased beyond the critical thicknesses, h_c, previously found for InAs QWs grown with As-based barriers ($h_c \sim 4$ nm for $In_{0.75}Al_{0.25}As$ [2] and $h_c \sim 7$ nm for $In_{0.81}Al_{0.19}As$ [9]). Finally, a top cladding layer of 10 nm $In_xGa_{1-x}As$ and a 120-nm-thick $In_{0.81}Al_{0.19}As$ top barrier layer were grown to complete the QW structure, as depicted in Fig. 1(a).

TABLE I. Highest quality samples from each In concentration series depicted in Fig. 1(b) with relevant properties listed. Cladding misfit is calculated using the formula $f = (a_{\text{barrier}} - a_{\text{cladding}})/a_{\text{cladding}}$.

Sample	x conc. of $In_xGa_{1-x}As$	QW thickness t_{QW} (nm)	Cladding Misfit (%)
Sample A	0.70	18	0.78
Sample B	0.72	16	0.64
Sample C	0.74	14	0.50
Sample D	0.81	4	0.03

Low temperature electron transport measurements were carried out utilizing a Quantum Design Physical Property Measurement System equipped with a magnet capable of generating fields up to 14 T. Sample resistance was determined using low frequency ac lock-in measurements with an ac excitation of 1 μA. Samples were measured using the van der Pauw (vdP) configuration to determine which samples had the highest mobility based on the In concentration in the cladding layer and the QW thickness, t_{QW}. These samples were created by cleaving the QWs into approximately square pieces prior to soldering In-Sn contacts onto the corners and annealing for 15 min at 250 °C. The highest mobility samples were fabricated into Hall bars with the long axis oriented along the $[1\bar{1}0]$. The mesa was formed using an etchant of H_2SO_4:H_2O_2:H_2O (1:8:120). Next, NiAuGe contacts were deposited and annealed at 450 °C for 120 s under forming gas to create ohmic contacts between the NiAuGe and the quantum well. A 30 nm Al_2O_3 gate dielectric was deposited using atomic layer deposition. Vias were defined to the NiAuGe contact pads, by etching through the dielectric. Finally, a layer of Ti/Au was deposited to fill the vias and form the top gate, enabling control of the carrier concentration within the QW. The fabricated Hall bar has an arm spacing of 740 μm and a width of 80 μm. These samples were used for gated magnetotransport measurements and characterization of the thermal dependence of the Shubnikov–de Haas (SdH) oscillations. Additionally, Rashba measurements were conducted utilizing a magnetic field modulation technique with two separate solenoids. The larger solenoid provides a dc magnetic field, while the smaller solenoid provides a small ac field, enabling the direct measurement of dR_{xx}/dB and d^2R_{xx}/dB^2.

III. RESULTS AND DISCUSSION

A. Tuning cladding layer properties

Magnetotransport measurements were performed on four series of samples with $In_{0.81}Al_{0.19}As$ barrier layers and

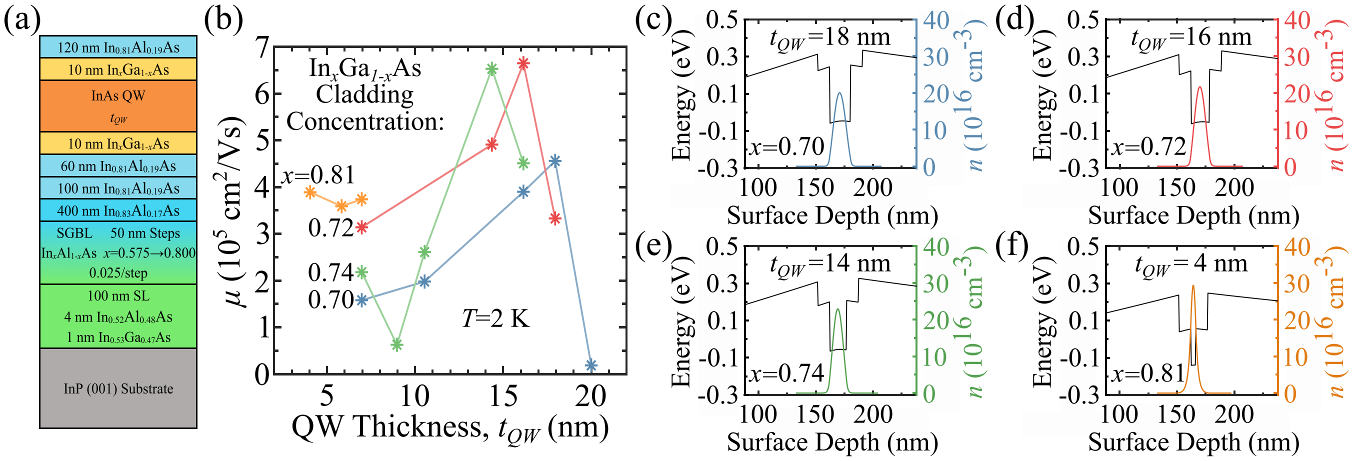

FIG. 1. (a) Schematic representation of InAs QW layer structure. (b) van der Pauw mobilities for four series of samples with differing strain levels in the $In_xGa_{1-x}As$ cladding layers and QW thicknesses (t_{QW}). The corresponding carrier density for each sample is depicted in Fig. S2 of the Supplemental Material [13]. (c)–(f) 1D Schrödinger-Poisson simulations [14] calculated for the highest mobility QW structure (see Table I for detailed properties) from each series of $In_xGa_{1-x}As$. As QW thickness decreases, the percentage of carriers confined in the InAs layer is reduced.

$In_xGa_{1-x}As$ cladding layers. The In concentration (x) of the cladding layer was varied for each series with x set to 0.70, 0.72, 0.74, or 0.81, changing the tensile strain present in the cladding layer. Additionally, the quantum well thickness, t_{QW}, was varied to determine whether strain compensation could enable the growth of thicker InAs QWs. These samples were wired in the vdP geometry and magnetic field sweeps were utilized to extract the relationship between the In concentration in the cladding layer, the maximum thickness of the QW, and the mobility of the QW, as depicted in Fig. 1(b). The samples included InAs QWs grown on $In_{0.81}Ga_{0.19}As$ (which has a misfit of only 0.03%, as defined in Table I) cladding layers with thicknesses ranging from $t_{QW} = 4$ to 7 nm. These samples enable us to compare our QWs with other state-of-the-art QWs as previous growths of InAs on $x = 0.75$ In-containing active regions were limited to a thickness of 4 nm [2] and growth of InAs layers on $x = 0.81$ In-containing active regions were limited to a thickness of 7 nm [9]. We observe minimal change in mobility as we increase t_{QW} for the $x = 0.81$ series. However, this is partially due to lack of control over the carrier concentration present in the QW and slight differences in thermal desorption temperatures, which can translate to variance in the QW mobility. Gated Hall bar measurements (not shown) demonstrated that the peak gated mobility of the sample with $t_{QW} = 7$ nm is greater than that of the $t_{QW} = 4$ nm sample, as expected from the results of Benali [9].

After studying the samples grown on $In_{0.81}Ga_{0.19}As$ cladding layers, the In content in the cladding layers was reduced. All of the 7-nm-thick QWs grown on strained cladding layers had lower mobilities relative to the samples grown on $In_{0.81}Ga_{0.19}As$. This may result from the increased alloy disorder scattering present as the In concentration, x, of the cladding layers is reduced. Previous work on InGaAs QWs has demonstrated that alloy disorder scattering plays an important role in the maximum achievable sample mobility [15,16].

As the QW thickness is increased beyond 7 nm, the measured vdP mobility generally increases in all of the samples until a peak mobility is achieved. To better understand this relationship, we utilized a 1D Schrödinger-Poisson simulation [14] to calculate the band structure and carrier concentrations for the highest mobility sample from each In concentration series measured in Fig. 1(b) (the structural properties of these selected samples are summarized in Table I). The results can be seen in Figs. 1(c)–1(f). By increasing QW thickness, the percentage of 2DEG contained within the InAs layer increases. The 18 nm InAs layer contains 97.2% of the charge carriers, the 16 nm well contains 96.8%, and the 14 nm well contains 95.0%. On the other hand, for the 4-nm-thick QW, the percentage of the carrier density residing within the InAs layer drops to 50.2%. These simulations demonstrate that 2DEG confinement has a strong dependence on the width of the InAs layer. Additionally, these simulations show that, by increasing QW thickness, the effects of interfacial roughness and alloy disorder scattering may be reduced as the carriers in thinner wells, like the 4 nm QW, reside much closer to the InGaAs/InAlAs regions. This explains the relationship between increasing t_{QW} and the measured QW mobilities in Fig. 1(b).

After the peak mobility is achieved, a sharp drop off in mobility is observed. It is interesting to note the peak mobility position shifts to thicker QWs as the cladding layer lattice misfit is increased [misfit is defined as $f = (a_{\text{barrier}} - a_{\text{cladding}})/a_{\text{cladding}}$, where a_{cladding} is the cladding layer lattice constant and a_{barrier} is the barrier layer lattice constant], indicating a correlation between the misfit of the cladding layer and the peak mobility. This relationship suggests that the drop in mobility is likely caused by relaxation of the InAs QW, similar to the growth of a 6 nm QW on an $x = 0.75$ In-containing active region grown by Hatke *et al.* [2]. Additionally, this relationship demonstrates that the $In_xGa_{1-x}As$ cladding layers are effectively offsetting the lattice constant mismatch between the InAs layer and the $In_{0.81}Al_{0.19}As$ barrier layers, delaying the onset of QW relaxation, as intended for strain

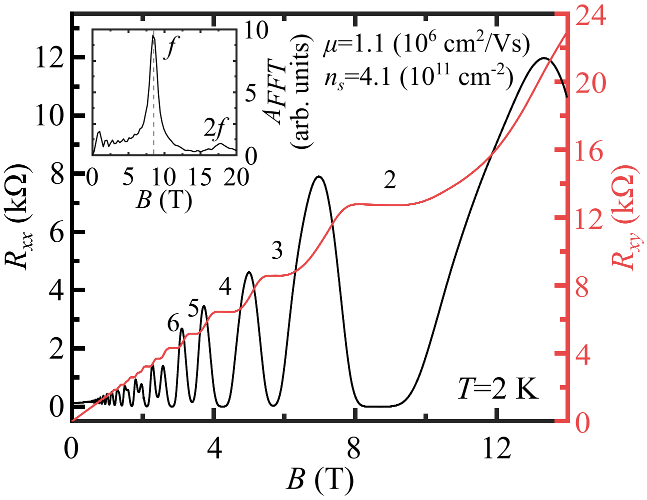

FIG. 2. Magnetotransport results of Sample B. Clear oscillations are present in R_{xx} and low field R_{xy} is linear indicating single channel transport. Inset: FFT of background-removed oscillations from low field R_{xx} measurements. A single peak and its harmonic are detected confirming single channel transport.

compensated structures [10–12]. The peak mobility found for the $In_{0.70}Ga_{0.30}As$ cladding layers is much lower than the peak mobility determined for either the $In_{0.72}Ga_{0.28}As$ or $In_{0.74}Ga_{0.26}As$ series of QWs. We interpret this to be a result of lattice relaxation and dislocation formation as reported by Hatke *et al.* [2] caused by the larger misfit of the $In_{0.70}Ga_{0.30}As$ cladding layers.

B. Gated transport measurements

The longitudinal and Hall resistance of the highest mobility sample, Sample B (see characteristics in Table I), are depicted in Fig. 2. Voltage was applied to the top gate to set the carrier concentration to 4.1×10^{11} cm^{-2}. At this carrier concentration, the sample mobility was measured to be $\mu = 1.14 \times 10^6$ cm^2/V s. At low fields, the Hall effect is found to be linear and, at high fields, the longitudinal resistance reaches 0 while the Hall resistance plateaus at quantized resistance values, indicating that no parallel transport channels are present in the QW structure. We confirm single channel transport utilizing SdH oscillations, which are well developed in the low field R_{xx} trace. Carrier concentration is extracted from the SdH oscillations by removing the background of R_{xx} using a linear fit. The resulting oscillations are Fourier transformed and the result is depicted in the inset of Fig. 2. The single peak and its harmonic in the FFT indicate that one transport channel is contributing to the SdH oscillations observed. We extracted the frequency of the inverse field oscillations and used the Onsager relation [17] to relate the frequency of the oscillations to the 2D carrier density of the transport channel. We found $n_{SDH} = 4.06 \times 10^{11}$ cm^{-2}, which agrees with the carrier concentration extracted from the Hall measurement.

Magnetotransport measurements were taken at a wide range of gate voltages for the highest mobility sample from each of the $x = 0.72$, 0.74, and 0.81 $In_xGa_{x-1}As$ series and the results are depicted in Fig. 3(a). By applying voltage to the top gate, we are able to modulate the carrier density within the QWs. The enhancement of mobility with increasing carrier density is due to better screening of charged defects, reducing the effects of Coulomb scattering [18]. Sample B (a 16 nm QW) shows the highest mobility of all of the samples studied and by increasing the carrier concentration within the well we are able to increase the mobility to a maximum of $\mu = 1.16 \times 10^6$ cm^2/V s, which is believed to be the highest mobility recorded for any InAs QW grown on an InP substrate that we can find in the literature [2]. The maximum mobility occurs at a carrier density of $n_s = 4.2 \times 10^{11}$ cm^{-2}. This represents a nearly 20% increase in mobility when compared to the record breaking QW grown by Hatke *et al.* [2] for a similar carrier density. The sample with the next highest mobility is Sample C (a 14 nm QW), with a maximum recorded mobility of $\mu = 6.85 \times 10^5$ cm^2/V s. The difference between the maximum attainable mobilities of sample B and sample C likely relates to the onset of relaxation. As shown by Hatke *et al.* the increase of the InAs layer from 4 nm to 6 nm led to a halving of the mobility [2]. The thickness of the QW in sample C may have exceeded the critical thickness of InAs by 3–4 nm, leading to subsequent relaxation and a large reduction in QW mobility. The relationship of the carrier density to the mobility beyond the peak for both the $In_{0.72}Ga_{0.28}As$ QW

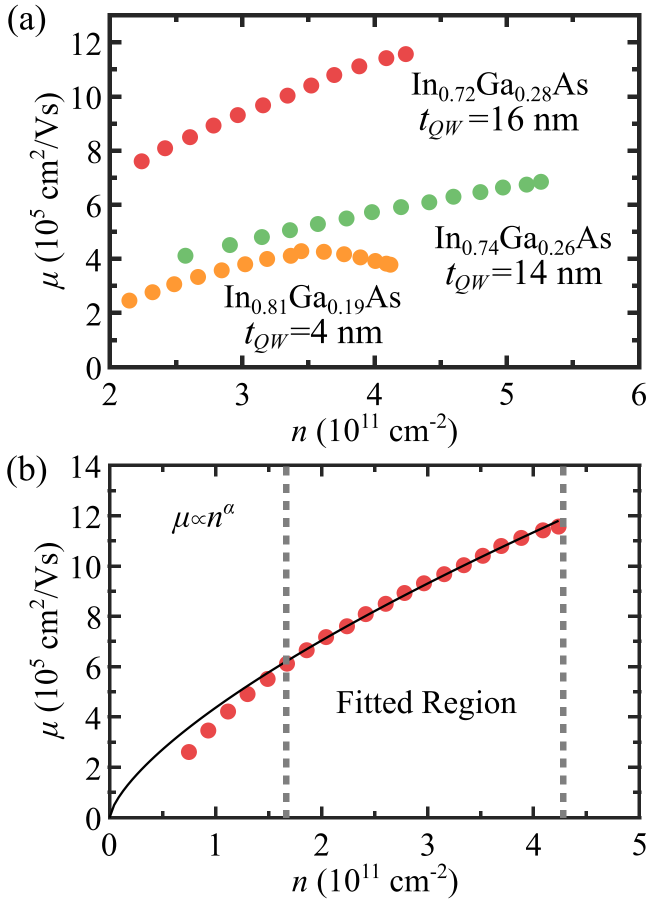

FIG. 3. (a) Mobility vs carrier density for the highest mobility samples from the $x = 0.72$, 0.74, and 0.81 $In_xGa_{1-x}As$ series measured in Fig. 1(b). (b) Extended mobility vs carrier density for Sample B, the highest mobility QW measured. The black line is a power-law fit using the expression $\mu \propto n_s^\alpha$.

and the $In_{0.74}Ga_{0.26}As$ QW is not depicted in Fig. 3(a), but is further discussed in the Supplemental Material, Fig. S4 [13].

To further understand the limits to the carrier mobility in Sample B, we studied the relationship between carrier density and mobility over a larger number of carrier concentrations as depicted in Fig. 3(b). By tuning the top gate voltage between −0.9 V and +0.1 V, we are able to modulate the carrier density from 7.5×10^{10} cm^{-2} up to 4.2×10^{11} cm^{-2}. In high-mobility two-dimensional systems the carrier mobility typically shows a power-law dependent relationship with the carrier density [19], $\mu \propto n_s^{\alpha}$. For the case of 2D carriers with 3D impurities and strong screening ($q_{TF} \gg 2k_F$, where q_{TF} is the Thomas-Fermi wave vector and k_F is the Fermi wave vector), $\alpha = 0.5$, and for the case of 2D carriers with 3D impurities and weak screening ($q_{TF} << 2k_F$), $\alpha = 1.5$. Using a log-log plot for the relationship between μ and n_s, we fit the slope of the data between $n_s = 1.6 \times 10^{11}$ and $n_s = 4.2 \times 10^{11}$. We extract $\alpha = 0.69$, which lies in between the two expected values of α. This intermediate value of α suggests that the mobility in this regime is limited by scattering from nearby background charged impurities. Similar values have been observed previously in both InAs QWs grown on InP substrates [20] and InAs QWs grown on GaSb substrates [3].

C. Extracting quantum lifetime

Quantum lifetime has been suggested as a predictor of the strength of fractional quantum Hall states and provides insight into the prevalent scattering mechanisms affecting transport [21]. To extract the quantum transport properties of Sample B (the 16 nm QW), we measured the longitudinal resistivity, ρ_{xx}, at a series of low temperatures ranging from 2 K to 20 K. A smooth polynomial was used to remove the resulting background. The resulting traces are depicted in Fig. 4(a). The oscillation amplitude decreases as the temperature is increased as a result of larger energy averaging occurring around the Fermi energy and can be described by the resistivity function derived by Isihara and Smrčka [22–24]:

$$\frac{\rho_{xx}}{\rho_o} = 1 + 4e^{-\pi/\omega_c\tau_q}\frac{X}{\sinh(X)}\cos\left(2\pi\frac{hn}{2qB} + \pi\right), \qquad (1)$$

where ρ_o describes the zero field resistivity, τ_q is the quantum lifetime, ω_c is the cyclotron frequency, defined as $\omega_c = qB/m^*$, X is the thermal dependence term, defined as $X = 2\pi^2 k_B T/\hbar\omega_c$, T is the temperature, n is the carrier concentration, and $B = \mu_o H$, where μ_o is the vacuum permeability and H is the applied field. The only temperature dependent term in Eq. (1) is the $X/\sinh(X)$ term. This allows us to extract the effective mass by plotting $\ln[\Delta\rho_{xx}T_o/(\bar{\rho}_{xx}T)]$ against T, as depicted in Fig. 4(b) for specific field values [25]. In this equation, $\Delta\rho_{xx}$ is the amplitude of the oscillation, $\bar{\rho}$ is the magnitude of the nonoscillatory background, and T_o is the temperature at which the lowest field sweep was conducted [25]. We extract the oscillation amplitude of multiple valleys and peaks before the onset of spin-splitting and selected results are depicted across multiple different temperatures in Fig. 4(b). The effective mass is found by fitting the data with $-\ln[\sinh(2\pi^2 k_B T m^*/\hbar qB)]$ and an offset [26]. The results of the fit are also displayed in 4(b). We determine $m^* = (0.031 \pm 0.002)m_e$, which agrees well with values found in the literature [20]. The inset of Fig. 4(c) depicts the extracted effective mass values for different magnetic field intensities.

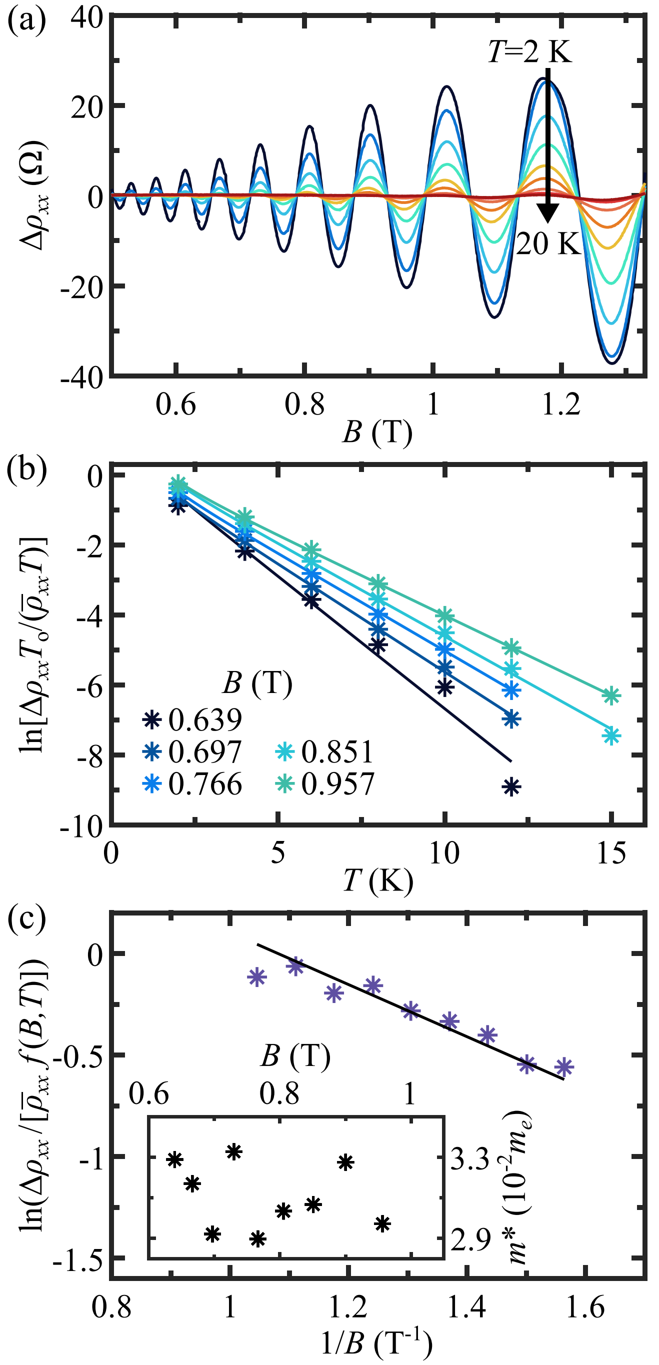

FIG. 4. (a) Thermal damping of SdH oscillations in ρ_{xx} after background has been subtracted by a smooth polynomial fit. (b) $\ln[\Delta\rho_{xx}T_o/(\bar{\rho}_{xx}T)]$ vs T for selected field amplitudes. Lines correspond to fits of data with $-\ln[\sinh(2\pi^2 k_B T m^*/\hbar qB)]$, enabling extraction of m^*. (c) $\ln(\Delta\rho_{xx}/[\bar{\rho}_{xx}f(B,T)])$ vs $1/B$ at 2 K. The slope of the fitted black line is inversely proportional to the quantum lifetime. Inset: extracted m^* values for varying B field positions from (b).

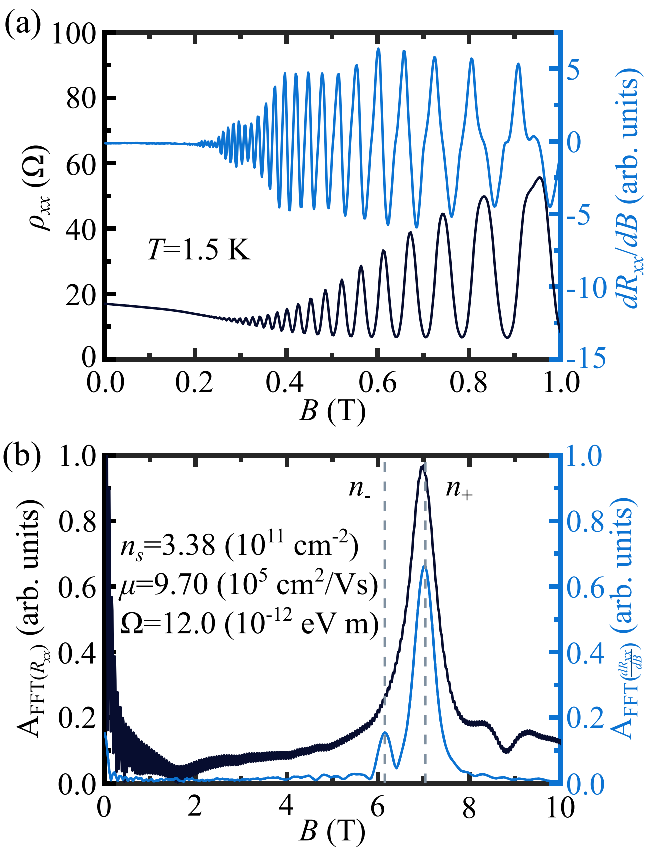

FIG. 5. (a) *Left axis:* response of ρ_{xx} to an applied magnetic field. *Right axis:* modulated magnetic field measurement of dR_{xx}/dB showing beating patterns indicative of spin splitting. (b) *Left axis:* FFT of the background removed ρ_{xx} data shown in (a) with a single peak evident. *Right axis:* FFT of the dR_{xx}/dB depicting two spin split peaks, labeled n_- and n_+. Vertical dashed gray lines have been added as guides to the eye.

Utilizing the extracted effective mass we can now determine the quantum lifetime term, τ_q, by plotting $\ln(\Delta\rho_{xx}/[\bar{\rho}_{xx} f(B,T)])$ against the inverse field, where $f(B,T) = 2\pi^2 k_B T/\hbar\omega_c/\sinh(2\pi^2 k_B T/\hbar\omega_c)$. The results are depicted in Fig. 4(c). A single parameter linear fit can be applied to the data. The y intercept is set to equal ln(4) based on work by Coleridge [27] and the slope of the line corresponds to slope $= -\pi m^*/q\tau_q$ [3]. We find $\tau_q = 0.45$ ps, which gives us a Dingle ratio of $\tau_t/\tau_q = 45$, where $\tau_t = \mu m^*/q$ is defined as the scattering time. Similar Dingle ratios have been previously observed in InAs QWs grown on GaSb substrates [4] with the same carrier concentration. The large difference in time constants is not unexpected as τ_t is primarily impacted by large angle scattering events. τ_q, on the other hand, is affected equally by all scattering events [28,29].

D. Determining spin-orbit coupling parameter

Both standard Hall effect measurements [2–4,30,31] and a magnetic field modulation technique [32] were employed to quantify the spin-orbit coupling in the 16 nm InAs QW (Sample B). The magnetoresistance oscillations of ρ_{xx} in response to the applied field are clearly visible in Fig. 5(a). A smooth polynomial fit was used to remove the background of the resistivity data. However, when the FFT is taken, as depicted in black in Fig. 5(b), only a single peak is evident. The lack of a split peak may be due to a weak Rashba response. To further investigate any potential Rashba splitting and to improve measurement sensitivity, the modulated magnetic field technique was utilized to directly measure dR_{xx}/dB and d^2R_{xx}/dB^2. A secondary solenoid, collinear with the primary dc field-generating solenoid, provided a small ac field in addition to the dc field. The ac field utilized to measure dR_{xx}/dB had a magnitude on the order of 1.6 mT and a frequency of 33 Hz. The resulting dR_{xx}/dB signal is depicted versus the applied static field in light blue in Fig. 5(a) [32]. The top gate voltage was kept at $V_g = 0$ V and the sample carrier density was measured to be 3.38×10^{11} cm^{-2}, corresponding to a mobility of 9.70×10^5 cm^2/V s. A clear beating pattern is present in the low field oscillation data. The FFT of the low field oscillations is depicted in Fig. 5(b) in light blue. Two peaks appear, nearly equal in frequency, arising from spin splitting [30,31,33,34].

To quantify the peak splitting, we switch to units of inverse field where the oscillations are periodic. Next, an FFT is taken of the oscillations. The result of the Fourier transform is displayed in Fig. 5(b). The two spin-split channels, labeled n_- and n_+, are highlighted by the vertical dashed lines. The frequency corresponding to the peak of each channel is extracted and can be converted to the carrier density utilizing the Onsager relation to get $n_i = qf_i/h$ [17], where $i = +, -$. We can extract the total carrier density, $n_T = n_+ + n_- = 3.2 \times 10^{11}$ cm^{-2}, giving good agreement with the carrier density measured by Hall transport. From the density of n_+ and n_- we can now extract the total spin-orbit coupling (SOC) parameter, Ω, using the relationship [33,35]

$$\Omega = \frac{\Delta n \hbar^2}{m^*}\sqrt{\frac{\pi}{2(n_T - \Delta n)}}, \tag{2}$$

where $\Delta n = n_+ - n_-$. Using Eq. (2) we find $\Omega = 12.0 \times 10^{-12}$ eV m. This value is similar to the Rashba parameters found for InAs QWs in literature [2,3,36], suggesting that the inherent asymmetry in the structure provides a small built-in electric field to the quantum well. Additionally, we can extract the spin-orbit length using $l_{SO} = \frac{1}{\Delta n}\sqrt{(n_T - \Delta n)/2\pi}$ [2,37]. We find a spin-orbit length of $l_{SO} = 102$ nm. This value is similar to the l_{SO} values found by Hatke *et al.* despite the lack of an applied electric field [2].

IV. CONCLUSION

In conclusion, we have demonstrated the advantages of utilizing strain compensation in InAs QWs grown on mismatched InP substrates. The addition of tensile strain in the InGaAs cladding layer increases the critical thickness of the InAs well, enabling t_{QW} to approach the QW thickness of InAs grown on nearly lattice-matched GaSb substrates. By increasing the thickness of the QW we demonstrated, utilizing 1D Schrödinger-Poisson simulations, that the percentage of the 2DEG state contained within the InAs layer increases from 50% up to 97% for our thickest InAs QW samples.

Magnetotransport measurements indicated that the lower bound of the In concentration in our 10-nm-thick InGaAs cladding layers is $x = 0.72$. When the In concentration was lowered beyond $x = 0.72$, the QW mobility dropped for all thicknesses of the QW. Our $In_{0.72}Ga_{0.28}As$ QW with

$t_{QW} = 16$ nm showed the highest mobility with a record-breaking carrier mobility of $\mu = 1.16 \times 10^6$ cm^2/V s with $n_s = 4.2 \times 10^{11}$ cm^{-2}. Next, we used the temperature dependence of the SdH oscillations to extract the effective mass and quantum lifetime, finding $m^* = 0.031\, m_e$ and $\tau_q = 0.45$ ps, which is consistent with previously measured values. Finally, utilizing a modulated field measurement we were able to extract the SOC parameter $\Omega = 12.0 \times 10^{-12}$ eV m and the spin-orbit length $l_{SO} = 102$ nm. This work demonstrates the potential of intentionally incorporating strain into the QW cladding layers to maximize the critical thickness of the QW region for InAs QWs grown on mismatched InP substrates.

ACKNOWLEDGMENTS

The authors acknowledge financial support of the growth and characterization of these quantum wells by the US Department of Energy under Award No. DE-SC0019274 and the UK Science and Technology Facilities Council under Award No. ST/Y005074/1. We acknowledge the use of the shared facilities of the NSF Materials Research Science and Engineering Center (MRSEC) at the University of California Santa Barbara (Grant No. DMR 2308708) and the fabrication facilities of the UCSB Nanofabrication Facility, an open access laboratory.

---

[1] C. R. Pidgeon, D. L. Mitchell, and R. N. Brown, Interband magnetoabsorption in InAs and InSb, Phys. Rev. **154**, 737 (1967).

[2] A. T. Hatke, T. Wang, C. Thomas, G. C. Gardner, and M. J. Manfra, Mobility in excess of 10^6 cm^2/Vs in InAs quantum wells grown on lattice mismatched InP substrates, Appl. Phys. Lett. **111**, 142106 (2017).

[3] C. Thomas, A. T. Hatke, A. Tuaz, R. Kallaher, T. Wu, T. Wang, R. E. Diaz, G. C. Gardner, M. A. Capano, and M. J. Manfra, High-mobility InAs 2DEGs on GaSb substrates: A platform for mesoscopic quantum transport, Phys. Rev. Mater. **2**, 104602 (2018).

[4] T. Tschirky, S. Mueller, C. A. Lehner, S. Fält, T. Ihn, K. Ensslin, and W. Wegscheider, Scattering mechanisms of highest-mobility InAs/Al$_x$Ga$_{1-x}$Sb quantum wells, Phys. Rev. B **95**, 115304 (2017).

[5] J. Shabani, M. Kjaergaard, H. J. Suominen, Y. Kim, F. Nichele, K. Pakrouski, T. Stankevic, R. M. Lutchyn, P. Krogstrup, R. Feidenhans'l, S. Kraemer, C. Nayak, M. Troyer, C. M. Marcus, and C. J. Palmstrøm, Two-dimensional epitaxial superconductor-semiconductor heterostructures: A platform for topological superconducting networks, Phys. Rev. B **93**, 155402 (2016).

[6] B. Shojaei, A. C. C. Drachmann, M. Pendharkar, D. J. Pennachio, M. P. Echlin, P. G. Callahan, S. Kraemer, T. M. Pollock, C. M. Marcus, and C. J. Palmstrøm, Limits to mobility in InAs quantum wells with nearly lattice-matched barriers, Phys. Rev. B **94**, 245306 (2016).

[7] S. Mueller, C. Mittag, T. Tschirky, C. Charpentier, W. Wegscheider, K. Ensslin, and T. Ihn, Edge transport in InAs and InAs/GaSb quantum wells, Phys. Rev. B **96**, 075406 (2017).

[8] C. Mittag, M. Karalic, S. Mueller, T. Tschirky, W. Wegscheider, O. Nazarenko, M. V. Kovalenko, T. Ihn, and K. Ensslin, Passivation of edge states in etched InAs sidewalls, Appl. Phys. Lett. **111**, 082101 (2017).

[9] A. Benali, P. Rajak, R. Ciancio, J. R. Plaisier, S. Heun, and G. Biasiol, Metamorphic InAs/InGaAs QWs with electron mobilities exceeding 7×10^5 cm^2/Vs, J. Cryst. Growth **593**, 126768 (2022).

[10] C. P. Seltzer, S. D. Perrin, M. C. Tatham, and D. M. Cooper, Zero-net-strain multiquantum well lasers, Electron. Lett. **27**, 1268 (1991).

[11] T. Tsuchiya, M. Komori, R. Tsuneta, and H. Kakibayashi, Investigation of effect of strain-compensated structure and compensation limit in strained-layer multiple quantum wells, J. Cryst. Growth **145**, 371 (1994).

[12] C. W. Tu, X. B. Mei, C. H. Yan, and W. G. Bi, Growth and characterization of strain-compensated InAsP/GaInP and InGaAs/GaInP multiple quantum wells, Mater. Sci. Eng. B **35**, 166 (1995).

[13] See Supplemental Material at http://link.aps.org/supplemental/10.1103/PhysRevMaterials.9.054607 for additional measurement details and simulations, which includes Refs. [2–4,14,38,39].

[14] I.-H. Tan, G. L. Snider, L. D. Chang, and E. L. Hu, A self-consistent solution of Schrödinger–Poisson equations using a nonuniform mesh, J. Appl. Phys. **68**, 4071 (1990).

[15] F. Capotondi, G. Biasiol, D. Ercolani, and L. Sorba, Scattering mechanisms in undoped In$_{0.75}$Ga$_{0.25}$As/ In$_{0.75}$Al$_{0.25}$As two-dimensional electron gases, J. Cryst. Growth **278**, 538 (2005).

[16] J. T. Dong, Y. Gul, A. N. Engel, T. A. J. van Schijndel, C. P. Dempsey, M. Pepper, and C. J. Palmstrøm, Enhanced mobility of ternary InGaAs quantum wells through digital alloying, Phys. Rev. Mater. **8**, 064601 (2024).

[17] L. Onsager, Interpretation of the de Haas-van Alphen effect, London, Edinburgh, Dublin Philos. Mag. J. Sci. **43**, 1006 (1952).

[18] G. Bastard, *Wave Mechanics Applied to Semiconductor Heterostructures* (Halsted, New York, 1988).

[19] S. Das Sarma and E. H. Hwang, Universal density scaling of disorder-limited low-temperature conductivity in high-mobility two-dimensional systems, Phys. Rev. B **88**, 035439 (2013).

[20] J. Shabani, S. Das Sarma, and C. J. Palmstrøm, An apparent metal-insulator transition in high-mobility two-dimensional InAs heterostructures, Phys. Rev. B **90**, 161303(R) (2014).

[21] Q. Qian, J. Nakamura, S. Fallahi, G. C. Gardner, J. D. Watson, S. Lüscher, J. A. Folk, G. A. Csáthy, and M. J. Manfra, Quantum lifetime in ultrahigh quality GaAs quantum wells: Relationship to $\Delta_{5/2}$ and impact of density fluctuations, Phys. Rev. B **96**, 035309 (2017).

[22] A. Isihara and L. Smrčka, Density and magnetic field dependences of the conductivity of two-dimensional electron systems, J. Phys. C **19**, 6777 (1986).

[23] B. Laikhtman and E. L. Altshuler, Quasiclassical theory of Shubnikov-de Haas effect in 2D electron gas, Ann. Phys. (N.Y.) **232**, 332 (1994).

[24] T. Ihn, *Semiconductor Nanostructures* (Oxford University Press, New York, 2010).

[25] Z. Lei, C. A. Lehner, K. Rubi, E. Cheah, M. Karalic, C. Mittag, L. Alt, J. Scharnetzky, P. Märki, U. Zeitler, W. Wegscheider, T. Ihn, and K. Ensslin, Electronic g factor and magnetotransport in InSb quantum wells, Phys. Rev. Res. **2**, 033213 (2020).

[26] Z. Lei, E. Cheah, F. Krizek, R. Schott, T. Bähler, P. Märki, W. Wegscheider, M. Shayegan, T. Ihn, and K. Ensslin, Gate-defined two-dimensional hole and electron systems in an undoped InSb quantum well, Phys. Rev. Res. **5**, 013117 (2023).

[27] P. T. Coleridge, Small-angle scattering in two-dimensional electron gases, Phys. Rev. B **44**, 3793 (1991).

[28] S. Peters, L. Tiemann, C. Reichl, and W. Wegscheider, Gating versus doping: Quality parameters of two-dimensional electron systems in undoped and doped GaAs/AlGaAs heterostructures, Phys. Rev. B **94**, 045304 (2016).

[29] A. Gold, Scattering time and single-particle relaxation time in a disordered two-dimensional electron gas, Phys. Rev. B **38**, 10798 (1988).

[30] K.-H. Kim, H.-J. Kim, H. C. Koo, J. Chang, and S.-H. Han, Spin-orbit coupling in double-sided doped InAs quantum well structures, Appl. Phys. Lett. **97**, 012504 (2010).

[31] T. Y. Lee, J. Chang, M. C. Hickey, H. C. Koo, H.-J. Kim, S.-H. Han, and J. S. Moodera, Quantum well thickness dependence of Rashba spin-orbit coupling in the InAs/InGaAs heterostructure, Appl. Phys. Lett. **98**, 202504 (2011).

[32] S. N. Holmes, P. J. Newton, J. Llandro, R. Mansell, C. H. W. Barnes, C. Morrison, and M. Myronov, Spin-splitting in p-type Ge devices, J. Appl. Phys. **120**, 085702 (2016).

[33] S. Datta and B. Das, Electronic analog of the electro-optic modulator, Appl. Phys. Lett. **56**, 665 (1990).

[34] C. Gauer, M. Hartung, A. Wixforth, J. P. Kotthaus, B. Brar, and H. Kroemer, Zero-field spin-splitting in InAs/AlSb quantum wells, Surf. Sci. **361-362**, 472 (1996).

[35] G. Engels, J. Lange, T. Schäpers, and H. Lüth, Experimental and theoretical approach to spin splitting in modulation-doped $\mathrm{In}_x\mathrm{Ga}_{1-x}\mathrm{As}$/InP quantum wells for B → 0, Phys. Rev. B **55**, R1958 (1997).

[36] D. Grundler, Large Rashba splitting in InAs quantum wells due to electron wave function penetration into the barrier layers, Phys. Rev. Lett. **84**, 6074 (2000).

[37] F. Dettwiler, J. Fu, S. Mack, P. J. Weigele, J. C. Egues, D. D. Awschalom, and D. M. Zumbühl, Stretchable persistent spin helices in GaAs quantum wells, Phys. Rev. X **7**, 031010 (2017).

[38] B.-M. Nguyen, W. Yi, R. Noah, J. Thorp, and M. Sokolich, High mobility back-gated InAs/GaSb double quantum well grown on GaSb substrate, Appl. Phys. Lett. **106**, 032107 (2015).

[39] S. Osako, T. Hamano, N. Mori, C. Hamaguchi, S. Sasa, and M. Inoue, Magnetophonon and magneto-intersubband-scattering effects in InAs/AlGaSb heterostructures, Phys. B: Condens. Matter **249-251**, 740 (1998).